Growth of Zirconia Particles Made by Flame Spray Pyrolysis

Roger Mueller, Rainer Jossen, Hendrik K. Kammler, and Sotiris E. Pratsinis
Particle Technology Laboratory, Dept. of Mechanical and Process Engineering, Eidgenössiche Technische Hochschule (ETH, Swiss Federal Institute of Technology), CH-8092 Zurich, Switzerland

M. Kamal Akhtar
Research Center, Millennium Chemicals Inc., Glen Burnie, MD 21060

DOI 10.1002/aic.10272
Published online in Wiley InterScience (www.interscience.wiley.com).

The growth of ZrO_2 particles in spray flames is studied at production rates of 100 and 300 g/h by thermophoretic sampling (TS) and image analysis of transmission electron microscope (TEM) micrographs. At each TS location, the corresponding temperature of the particle-laden spray flame is measured along the centerline by Fourier transform infrared (FTIR) spectroscopy. The product powder is analyzed by nitrogen adsorption and TEM. The measured evolution of primary particle size distribution is presented and quantitatively explained, accounting for aerosol coagulation and sintering. The evolution of the average agglomerate size and number of primary particles per agglomerate is calculated and compared to TEM micrographs. © 2004 American Institute of Chemical Engineers *AIChE J,* 50: 3085–3094, 2004
Keywords: coagulation-sintering, aerosol dynamics, thermophoresis, agglomerate and primary particles, nanoparticles

Introduction

Flame spray pyrolysis (FSP) is one of the promising techniques for synthesis of a broad spectrum of functional inorganic nanoparticles because it overcomes the need for gaseous precursors that are required by the industrially established flame reactors for manufacture of fine-particle commodities. A number of materials have already been made by FSP from pure ZnO (Marshall et al., 1971) and Al_2O_3 (Sokolowski et al., 1977) to more complex mixed oxides and spinels (Laine et al., 1999, 2000) and even mixed noble metal–ceramic catalysts (Strobel et al., 2003). Although some systematic studies on the role of process parameters on the characteristics of product particles have been carried out (Mädler et al., 2002) and even scale-up of FSP has been addressed (Mueller et al., 2003, 2004a), this promising technique has been treated as a "black" box so far, relating input parameters to product powder characteristics. Essentially little is known on how droplets are converted to particles, given that *in situ* measuring of flame and particle characteristics is rather challenging in these particle-laden flames. Such data are needed to understand some of the intriguing FSP results such as the formation of solid or hollow Al_2O_3 by replacing air with O_2 as oxidant/dispersion gas (Tani et al., 1998, 2003) or Bi_2O_3 by controlling the composition of the precursor solution fed to FSP (Mädler and Pratsinis, 2002).

Synthesis of ZrO_2 particles is studied here because it is a basis material in catalysts, oxygen sensors, fuel cells, resistive heating elements, and even jewelry for its high oxygen ion conduction and high refractive index (Chraska et al., 2000; Gell, 1995; Gleiter, 1992; Mayo et al., 1999). Some FSP studies on ZrO_2 synthesis have been carried out already (Karthikeyan et al., 1997; Kilian and Morse, 2001; Limaye and Helble, 2002; 2003) but they have not addressed quantitatively the evolution of primary and agglomerate ZrO_2 particle size.

The objective of the present study is to investigate primary and agglomerate ZrO_2 particle growth *inside* spray flames at

Correspondence concerning this article should be addressed to S. E. Pratsinis at pratsinis@ptl.mavt.ethz.ch.

Table 1. Process Conditions and Product ZrO_2 Particle Characteristics

Parameter	Flame 1	Flame 2
Production rate, g/h	100	300
Liquid feed rate, mL/min	27.1	81.1
Precursor concentration, M	0.5	0.5
Dispersion gas flow rate, L/min	50	50
Total gas flow rate, L/min	77	170
Jet Reynolds number	10,400	23,000
Max. flame temperature, K	2610	2765
Adiabatic flame temperature, K	3765	5000
Flame height, cm	13	37
d_{pS} at filter, nm	15.3	26.7
d_{pBET} at filter, nm	12.0	25.8

relatively high production rates by thermophoretic sampling (TS) and transmission electron microscope (TEM) micrographs (Dobbins and Megaridis, 1987). The temperature history of the particles is recorded by Fourier transform infrared (FTIR) emission/transmission (E/T) spectroscopy (Best et al., 1986), a technique that has been used successfully in gas-fed flame reactors (Arabi-Katbi et al., 2001). These data are compared to a quantitative description of ZrO_2 particle growth, accounting for aerosol coagulation and sintering (Kruis et al., 1993) during FSP after evaluation of ZrO_2 sintering data from the literature.

Experimental

Apparatus and characterization

The spray pyrolysis unit consists of a commercially available external-mixing stainless-steel gas-assisted nozzle (970/4-S32; Schlick-Düsen, Gustav Schlick GmbH, Untersieman, Germany) having a capillary tube with an inner diameter of 0.5 mm and an annular gap with inner/outer diameter of 1.7/2.35 mm. The nozzle is surrounded by two stainless-steel annuli having inner/outer diameters of 18–19 and 20–25 mm, respectively (Mueller et al., 2003), resulting in an assumed average equivalent jet diameter d_n of 10 mm, which is used for modeling the spray. These annuli form a supporting or "pilot" diffusion flame by flowing 2 L/min CH_4 (≥99.5%; PanGas, Zurich, Switzerland,) through the inner and 4.5 L/min O_2 (>99.95%; PanGas) through the outer annulus. Additional sheath O_2 (15 L/min) is fed through a sintered metal plate ring surrounding the latter annulus. The nozzle/burner unit is moved by a positioning system (Unipos 110; Foehrenbach AG, Weinfelden, Switzerland) with an accuracy of 0.05 mm axially and laterally.

The ZrO_2 precursor, zirconium *n*-propoxide [$Zr(C_3H_7O)_4$, 70 wt % in *n*-propanol; ChemPur, Karlsruhe, Germany], is diluted in ethanol (EtOH, >99.8%; Fluka, Buchs, Switzerland) at a concentration $c = 0.5$ M. This precursor solution is fed by a precision piston pump (model 1000D; Isco Industries, Bend, OR) through the innermost capillary tube of the nozzle at feed rates S of 27.1 and 81.1 mL/min, resulting in ZrO_2 production rates of 100 (Flame 1) and 300 g/h (Flame 2) and adiabatic flame temperatures of 3785 and 5000 K, respectively (Table 1). That way the spray flame is stable, even though it is turbulent and the high-frequency flame instabilities reach a quasi-steady state. Oxygen is used as dispersion/oxidant gas at a flow rate of 50 L/min and passes through the first annular gap of the nozzle at a pressure drop of 1 bar across the nozzle tip.

The ZrO_2 particles are collected by a commercial jet filter unit (model FRR 4/1.2; Friedli AG, Burgdorf, Switzerland) consisting of four PTFE (polytetrafluoroethylene, Teflon)-coated Nomex baghouse filters (total surface area: 1.7 m^2) in a stainless-steel housing (2.3 m high and 0.5 m in diameter) that is connected with a 1-m-long inlet pipe (ID = 12 cm) with a cone-shaped open end over the nozzle/burner unit. Small samples (~ 1 g) of product particles are collected with the aid of a vacuum pump (model RE 16; Vaccubrand GmbH and Co., Wertheim, Germany) on a glass fiber filter (Whatmann GF/A) 150 mm in diameter. The filter is located in a stainless-steel holder sampling the product powder with a bypass connected to the inlet pipe 30 cm away from the filter housing (Mueller et al., 2003). Powders collected on the glass fiber filter were identical (same specific surface area and morphology) to those collected with the baghouse filters.

The powder specific surface area (SSA) is determined by N_2 adsorption (Tristar, Micromeritics Instruments Corp., Norcross, GA) from a five-point isotherm in the relative pressure range of 0.05 to 0.25 at 77.3 K (BET analysis). Before adsorption, the samples are degassed (Flow prep 060; Micromeritics Instruments) under N_2 atmosphere at 150°C for 1 h, to remove water bound to the particle surface from air moisture. Assuming monodisperse spherical ZrO_2 primary particles, the BET-equivalent average primary particle diameter d_{pBET} is calculated by $d_{pBET} = 6/(\rho_p SSA)$, where ρ_p is the density of tetragonal ZrO_2, 6.1 g/cm^3.

The integral centerline spray flame temperature is measured *in situ* by emission/transmission spectroscopy (Best et al., 1986) using a Fourier transform infrared (FTIR) spectrometer (model MB155S; Bomem Inc., Quebec, Canada) operating in the range of 6500–500 cm^{-1} with 32 cm^{-1} spectral resolution taking up to 3000 scans per temperature measurement. Two pairs of identical paraboloidal mirrors guide the IR beam through the flame and a 0.4 cm iris at the first focal point defines the beam diameter in the flame center (second focal point). Transmission and emission (radiance) spectra are collected with wide-band deuterated-triglycine–sulfate (DTGS) detectors. The temperature is determined by Normrad and ET analyses from hot CO_2 (2300 to 2200 cm^{-1}) and the reported temperature is the average of the two analyses (Kammler et al., 2002). The spray flame height is determined visually as the distance from the nozzle tip to the end of the luminous flame zone.

Thermophoretic sampling

Particle samples are collected by a thermophoretic sampler (Kammler, 2002) that rapidly moves a carbon-coated copper TEM grid (200 mesh; Plano GmbH, Wetzlar, Germany) to a precisely defined position in the spray flame (Dobbins and Megaridis, 1987). The residence time of the TEM grid inside the spray flame can be varied (typically 50 ms) and is calibrated along with its traveling time (4 ms across the flame) using a high-speed digital camera (model 4540; Kodak Ektapro, Rochester, NY). The TEM grid is held between two stainless-steel blades (0.0125 × 0.3 × 5 cm) leaving, however, a 0.2-cm-diameter hole at one side to expose the grid to the ZrO_2 aerosol. This grid holder with the TEM grid travels through a slotted cylindrical shield, which is 0.5 cm outside of the visible spray flame edge, to avoid disturbing the flame upstream of the

sampling point (Dobbins and Megaridis, 1987; Kammler, 2002).

The TEM analysis is carried out with a Hitachi H 600 and a Zeiss 912 Omega electron microscope both operated at 100 kV, using magnifications between 20 and 50K. The TEM micrographs from the filter powder are prepared from the powder as-is, dipping the TEM grid into the product powder. For each flame location as well as the product powder, typically 500–3000 primary particles are counted manually using the Optimas 6.51 (Media Cybernetics, Yorkville, IL) software. Statistical analysis of the data is performed according to Hinds (1999).

Theory

Aerosol dynamics

Assuming rapid droplet evaporation and zirconium *n*-propoxide oxidation, the product ZrO_2 particles grow by monomer–and cluster–cluster collisions, neglecting the spread of the primary and agglomerate size distribution. Thus, the evolution of the average primary and agglomerate particle diameters can be described by coagulation and sintering as in gas-fed flame aerosol reactors (Kruis et al., 1993), neglecting jet entrainment (Johanessen et al., 2000). Therefore, the particle number concentration N decreases by coagulation

$$\frac{dN}{dt} = -\frac{1}{2}\beta N^2 \rho_{gas} \tag{1}$$

where ρ_{gas} is the gas density at temperature T and β is the collision frequency function for Brownian coagulation given by the Fuchs interpolation function from the free-molecular to the continuum regime (Seinfeld, 1986). The effect of agglomerate structure in β is incorporated by replacing the particle diameter with the collision diameter (Kruis et al., 1993). A constant mass fractal dimension D_f of 1.8 is used, which is common for agglomerated particles generated by cluster–cluster aggregation in high-temperature aerosol processes (Schaefer and Hurd, 1990). Likewise, the evolution of the surface area of an agglomerate particle, a, is

$$\frac{da}{dt} = -\frac{1}{N}\frac{dN}{dt}a - \frac{1}{\tau_s}(a - a_e) \tag{2}$$

where τ_s is the characteristic sintering time for ZrO_2 and a_e is the equivalent surface area of a completely fused (spherical) agglomerate of volume v. Equation 2 shows that the surface area of an agglomerate particle increases by coagulation [first right-hand side (RHS) term] and decreases by sintering (second RHS term) and with $A = aN$ Eq. 2 becomes

$$\frac{dA}{dt} = -\frac{1}{\tau_s}(A - Na_e) \tag{3}$$

where A is the total particle area concentration (Koch and Friedlander, 1991). The average volume of an agglomerate particle is $v = V/N$. The primary particle diameter d_p, the number of primary particles per agglomerate n_p, and the agglomerate diameter d_a, are

$$d_p = \frac{6v}{a} \quad n_p = \frac{a^3}{36\pi v^2} \quad d_a = d_p(n_p^{1/D_f}) \tag{4}$$

Equations 1 and 3 can be further transformed as follows

$$\frac{dZ}{dt} = \frac{dZ}{dx}\frac{dx}{dt} = \frac{dZ}{dx}u \quad \text{where } Z = N, A \tag{5}$$

where u is the axial gas velocity profile of the spray as a function of height above the nozzle x, and is obtained from a correlation for turbulent jets issuing from a round nozzle (Bejan, 1984) corrected for the spray flame temperature

$$u = \begin{cases} u_0 \dfrac{T(x)}{T(0)} & x/d_n \le 5.27 \\ \dfrac{5.27u_0}{x/d_n}\dfrac{T(x)}{T(0)} & x/d_n > 5.27 \end{cases} \tag{6}$$

where d_n is the assumed average equivalent jet diameter (10 mm), $T(x)$ is the temperature at x and $T(0)$ is the gas reference temperature at $x = 0$ cm (298 K) of the nozzle. The gas exit velocity u_0 is calculated by the ratio of $4F/(\pi d_n^2)$, where the total gas flow rate F is 77 and 170 L/min for Flames 1 and 2, respectively, including the generation of gas by complete combustion of the liquid Zr-precursor and the EtOH solvent. Equations 1 and 3 are solved by VODPK software (Byrne, 1992) with the initial conditions ($x = 0$ and 5 cm for Flame 1 and $x = 0$ and 7.5 cm for Flame 2): $N = N_0 = [(S/1000)cN_A]/[F\rho_{gas}(0)]$; $V = V_0$; $A = A_0$, where N_0 is the initial monomer (molecule) concentration of ZrO_2; and A_0 and V_0 are the initial equivalent-sphere surface area and volume concentrations, respectively, of all ZrO_2 molecules. This model is attractive for its simplicity, computational efficiency, and accuracy for predicting the final particle diameter in gas phase processes, especially at high temperatures (within 10% of polydisperse models: Figure 7 by Spicer et al., 2002).

Droplet evaporation is assumed to be instantaneous because no hollow particles were observed in this process that would have indicated slow precursor evaporation (Kodas and Hampden-Smith, 1999). Nevertheless, thermophoretic sampling close to the nozzle indicated the presence of uncombusted droplets as discussed later. Instantaneous conversion of the precursor to ZrO_2 is justified because precursor could not be observed by FTIR in the flame (Mueller, 2003), no visible coloration of product particles by incomplete combustion (Kammler et al., 2001), and no splatter-like particles could be observed in SEM/TEM (Nakaso et al., 2003). The rapid evaporation and reaction assumptions are evaluated by examining particle formation to start at $x = 0$ cm or at $x = 5$ and 7.5 cm for Flames 1 and 2, respectively. The $x = 5$ or 7.5 cm locations correspond to 2.5 cm below the first TS particle sampling position for each production rate. The assumption of constant D_f hardly affects the estimated average primary particle size (Akhtar et al., 1994).

Characteristic sintering time

Expressions relating the characteristic time for sintering to temperature and primary particle size, are derived from the

so-called initial stage sintering models that describe the center-to-center approach and neck growth between two equal-sized spheres (Coblenz et al., 1980). The curvature between the spheres disappears when the ratio of the neck length x_n, to the initial sphere radius r_p ($=d_p/2$), reaches 0.83, which is considered as the completion of sintering (Kobata et al., 1991). For ZrO_2, grain boundary diffusion is the dominant sintering growth mechanism, which is three to four orders of magnitude faster than volume diffusion (Brossmann et al., 1999). Therefore, the characteristic sintering time for grain boundary diffusion can be expressed by (Coblenz et al., 1980)

$$\tau_s = 0.001703 \frac{RT\left(\frac{d_p}{2}\right)^4}{wD_b\gamma\Omega} \tag{7}$$

where R is the universal gas constant, $w = 5 \times 10^{-10}$ m is the grain boundary width (Brossmann et al., 1999), γ is the surface tension according to Rösner-Kuhn et al. (1999), $\Omega = 2.01998 \times 10^{-5}$ m^3/mol is the molar volume of zirconia, and D_b is the grain boundary diffusion coefficient for ZrO_2

$$D_b = D_0 \exp\left(\frac{-E}{RT}\right) \tag{8}$$

where D_0 is the grain boundary diffusion preexponential factor and E is the activation energy. Here, $D_0 = 9.73 \times 10^{-7}$ m^2/s (Madeyski and Smeltzer, 1968) and $E = 2.33 \times 10^5$ J/mol are selected after a detailed evaluation of these material properties (Mueller, 2003).

Results and Discussion

Zirconia spray flame characteristics

Increasing the liquid (solution) feed rate from 27.1 to 81.1 mL/min (which increases the ZrO_2 production rate from 100 to 300 g/h) increases the spray flame height from 13 to 37 cm. This increase of the liquid feed rate by a factor of 3 increases the supplied fuel energy to the spray by a factor of 3, thus prolonging the time for fuel combustion and nearly tripling the spray flame height (13 to 37 cm). Figure 1 shows integral (line-of-sight) centerline temperature profiles of these two particle-laden ZrO_2 spray flames. For both, the maximum temperature is measured close to the nozzle tip (for Flame 1 it is 2610 K at $x = 0.5$ cm and for Flame 2 it is 2765 K at $x = 2.5$ cm). The Flame 1 temperature decreases by about 110 K/cm up to $x = 12.5$ cm (end of the luminous part of the flame) and above that by 45 K/cm. The temperature of Flame 2 decreases by about 85 K/cm up to $x = 7.5$ cm, whereas above that by about 30 K/cm. The high temperature close to the nozzle tip results from the supporting CH_4/O_2 diffusion flame because visible spray ignition takes place at this location.

The measured temperatures are close to those of Mädler et al. (2002), who measured by FTIR a maximum temperature of 2620 K at $x = 0.7$ cm in a much smaller SiO_2 particle-laden spray flame using O_2 as dispersion gas at 1 bar pressure drop across the nozzle tip. Kilian and Morse (2001) measured ZrO_2 and Al_2O_3 spray flame temperatures optically from 2300 to 3000 K depending on precursor composition. Here, a temperature evaluation closer to the nozzle tip [$x < 0.5$ cm (Flame 1) and $x < 2.5$ cm (Flame 2)] by FTIR spectroscopy was not possible because the dense precursor droplet concentration resulted in considerable IR absorption and a weak signal-to-noise ratio. The flame temperature decreased by radiation and entrainment of sheath gas (15 L/min O_2), which dilutes and cools the spray flame. The measured temperature gradients are comparable to those in gas-fed flames, where up to 200 K/cm were measured in diffusion flames producing agglomerate and nonagglomerate SiO_2 (Mueller et al., 2004b) and about 100 K/cm in TiO_2 producing premixed flames (Kammler et al., 2003). Furthermore, the lines in Figure 1 are the regressions used in the calculations (Flame 1, solid line; Flame 2, broken line) based on a piecewise linear temperature profile (Mueller, 2003). Both temperature profiles are approximated to decrease linearly down to 500 K, followed by a constant temperature down to the bypass filter location at $x = 100$ cm, which is in agreement with thermocouple measurements on the glass fiber filter.

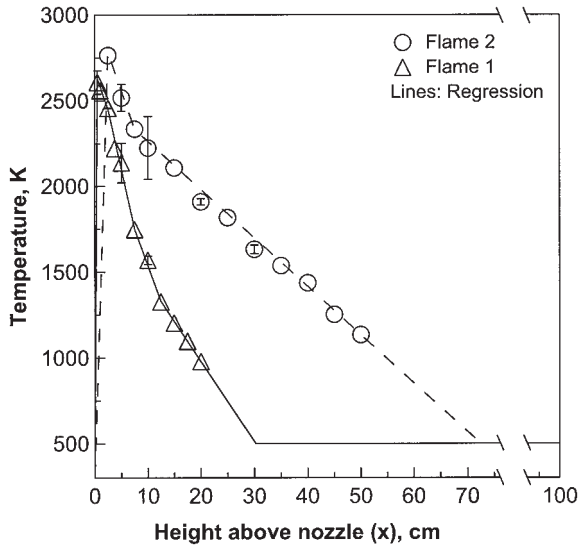

Figure 1. Flame temperature profiles of ZrO_2 particle-laden spray flames measured along the centerline by Fourier transform infrared (FTIR) spectroscopy for ZrO_2 production rates of 100 (triangles, Flame 1) and 300 g/h (circles, Flame 2) and their corresponding regression lines (Flame 1, solid line; Flame 2, broken line).

Formation and growth of FSP-made ZrO_2

In contrast to gas-fed flame aerosol reactors, with spray flames TS is only possible at locations where the droplets are completely evaporated, such as at and above $x = 7.5$ and 10 cm for Flames 1 and 2, respectively; otherwise, the carbon-coated TEM grids are destroyed by the burning droplets depositing on them. Therefore, monitoring the evolution of particle growth in the early stages of the spray flame was not possible.

Figures 2 and 3 show TEM micrographs from TS along the flame axis (x), as well as from the powder collected on the filter for both production rates. No hollow particles or shell fragments were observed throughout the process. The primary

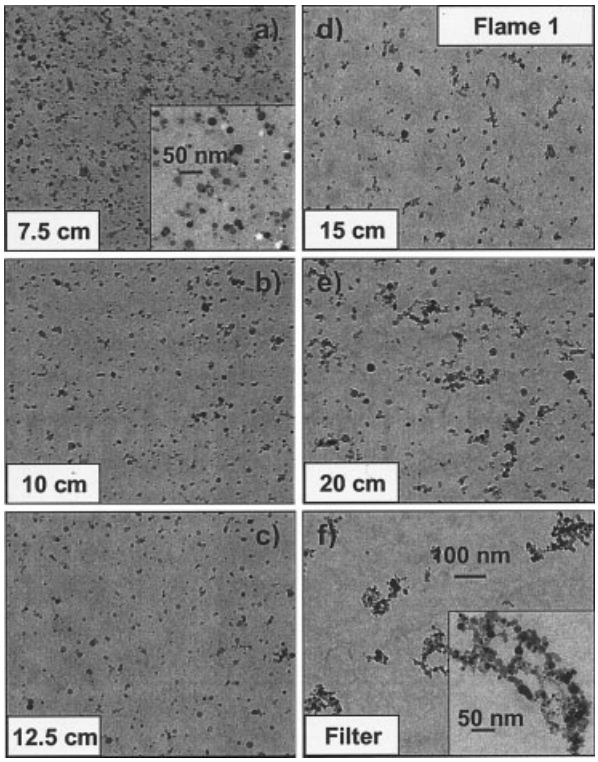

Figure 2. ZrO_2 particles collected by thermophoretic sampling at x = 7.5, 10, 12.5, 15, and 20 cm height above nozzle, and product powder (filter) at a production rate of 100 g/h (Flame 1).

particle size increases with increasing x for both production rates by gas phase or surface reaction, coagulation, and sintering as in gas-fed premixed flames (Arabi-Katbi et al., 2001; Kammler et al., 2003; Pratsinis et al., 2000). In the luminous part of the spray flames, single spherical particles are observed, whereas further downstream agglomeration of primary particles can be seen, starting approximately at x = 15 cm (Figure 2) for Flame 1 and at about x = 40 cm (Figure 3) for Flame 2. However, limited necking between those broadly sized primary particles is observed, indicating a low degree of agglomeration (detail TEMs in Figures 2 and 3). Similarly, agglomerates are observed in the powder collected on the filter where product particles made from Flame 1 consist of very small highly agglomerated particles as well as weakly agglomerated ones (Figure 2f). Only limited necking between the primary particles is observed for particles made from Flame 2 (Figure 3) without the small, highly agglomerated fraction that is observed for powder made in Flame 1. The temperatures of the spray flames are high enough (Figure 1) for complete particle coalescence and also the particle residence times are longer than the characteristic sintering time for ZrO_2 so that agglomerates are not observed in the luminous part of the spray. Further downstream, the temperature of Flame 1 is too low (1000 K at x = 20 cm) for complete particle coalescence, resulting in agglomerated product powder while the temperature of Flame 2 is still high enough (1400 K at x = 40 cm) for almost complete particle coalescence.

Primary particles made in Flame 2 are significantly larger than those made in Flame 1 at all locations and on the filter (Figures 2 and 3). Increasing the production rate by increasing the liquid feed rate results in a higher enthalpy content of the flame that leads to longer particle residence times at high temperatures (Figure 1), increasing the particle sintering rate, resulting in the formation of larger primary particles. Furthermore, the precursor concentration increases and therefore the ZrO_2 concentration leads to faster coagulation and therefore enhanced particle growth that increases the particle diameter, especially when complete coalescence takes place (Pratsinis, 1998).

Figure 4 shows the evolution of the primary particle size distribution (PPSD) obtained from TEM image counting (Figures 2 and 3) for Flames 1 (triangles) and 2 (circles). The PPSDs are shifted to larger sizes with increasing x similar to TiO_2 particle growth in gas-fed flames (Arabi-Katbi et al., 2001; Kammler et al., 2003). For both production rates, it is observed that the PPSDs become narrower with increasing x. This is different from gas-fed flames where the PPSDs become broader at increasing height above burner by possible inclusions of particles at different residence times and temperature

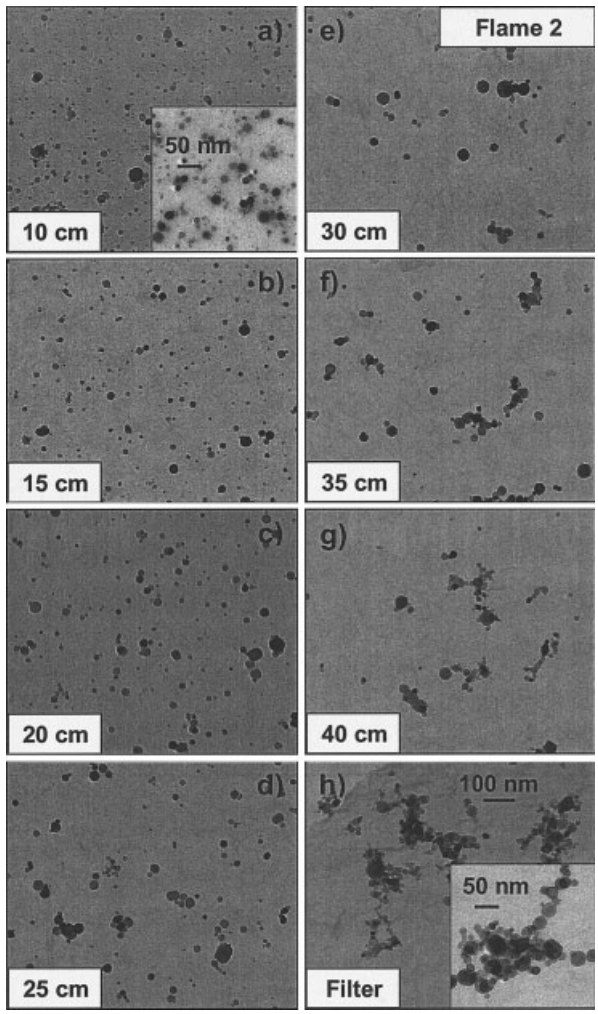

Figure 3. ZrO_2 particles collected by thermophoretic sampling at x = 10, 15, 20, 25, 30, 35, and 40 cm height above nozzle, and product powder (filter) at a production rate of 300 g/h (Flame 2).

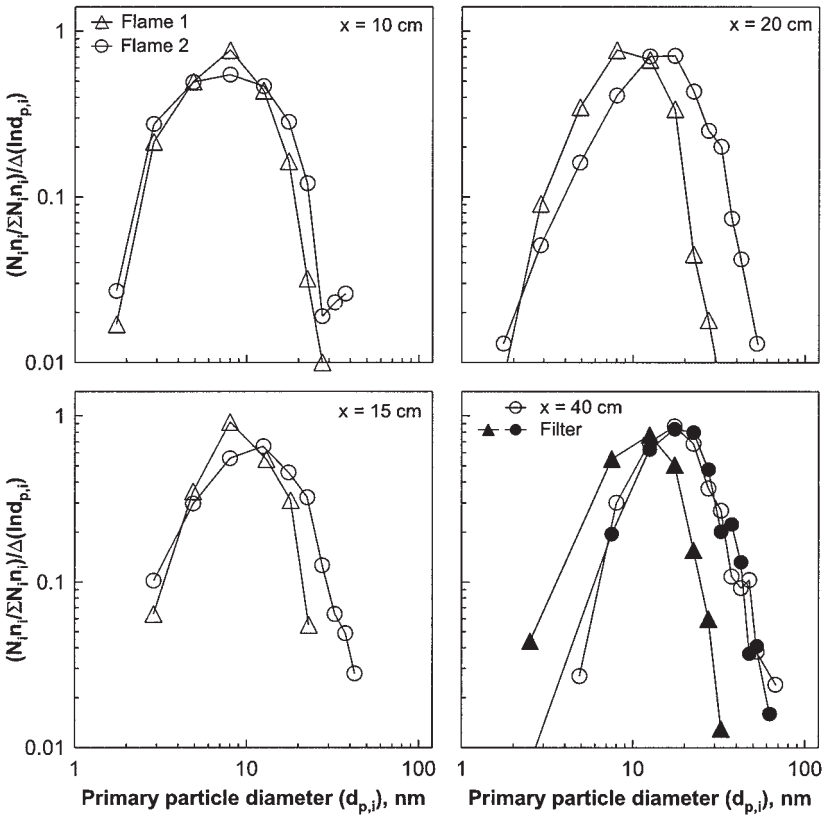

Figure 4. Evolution of the primary particle size distribution at x = 10, 15, 20, and 40 cm height above nozzle, and product powder (filter; Mueller et al., 2004a) for ZrO_2 production rates of 100 (triangle, Flame 1) and 300 g/h (circles, Flame 2).

histories in the sample (Arabi-Katbi et al., 2001). In contrast, in spray flames droplet evaporation, precursor release, and particle formation take place within the first part of the flame, leading to wide PPSDs as primary particles are formed at different locations within the flame having different residence times at high temperature, whereas further downstream, when the precursor is completely released from the droplets, particles grow by coagulation and sintering, thus decreasing the PPSD. Particles collected on the filter (Mueller et al., 2004a) typically exhibit different residence times as they are collected from various streamlines corresponding to different temperature and velocity profiles (Tsantilis et al., 2002); thus, the PPSD become slightly wider (Figure 4; σ_g = 1.63, Flame 2) compared to the last TS position (σ_g = 1.58, Flame 2) on the centerline of the spray.

The PPSDs are broader and shifted to larger average particle diameters as the production rate is increased from 100 to 300 g/h (Figure 4), which was also observed in the TEMs (Figures 2 and 3). The increase in powder production rate (by increasing the liquid feed rate) decreases the gas-to-liquid mass ratio (GLMR) increasing the mass median droplet diameter, $d_{50.3}$ (Mueller et al., 2003), thus increasing the time for complete droplet evaporation and precursor release leading to prolonged duration of particle formation and therefore leading to wider PPSDs. This also explains the narrower PPSDs found in gas-fed flames where the precursor is introduced in its gaseous form; thus, particle formation starts immediately when the precursor is entering the high-temperature zone.

Figure 5 shows the evolution [TS/TEM (open symbols) and BET (filled symbols)] of the Sauter mean primary particle diameter d_{pS} (Figures 2 and 3) as a function of x for (a) Flame 1 and (b) Flame 2 along with the theoretical model predictions (lines; see following section). The standard deviation of multiple reproduction (error bar) is typically so small (<3%) that it is smaller than the symbol in the figure. Increasing the powder production rate by increasing the liquid precursor feed rate increases both the mass concentration of the zirconia particles and the flame temperature (Figure 1). Higher flame temperatures and higher particle concentrations favor coagulation and complete sintering of the particles; thus, larger primary particle diameters are formed (Figure 5), consistent with particle synthesis in gas-fed flame reactors (Pratsinis, 1998).

The average primary particle diameters are comparable at x = 20 cm (d_{pS} = 13.6 nm) and the filter location (d_{pS} = 15.3 nm) for Flame 1 and at x = 40 cm (d_{pS} = 26.7 nm) and the filter location (d_{pS} = 26.7 nm) for Flame 2. This indicates that primary particle growth stops shortly after the particles leave the luminous part of the flame, resulting in agglomerates as observed by TEM (Figures 2 and 3). The primary particles collected on the filter for Flame 1 are smaller by about 60% than those made in Flame 2. This is consistent with a $(300/100)^{2/5}$ dependency on the mass or volume aerosol concentration of coagulation–coalescence dominated growth in the free molecular regime (Koch and Friedlander, 1991).

The corresponding BET-equivalent primary particle diameters (filled symbols in Figure 5) are similar (Flame 2) or

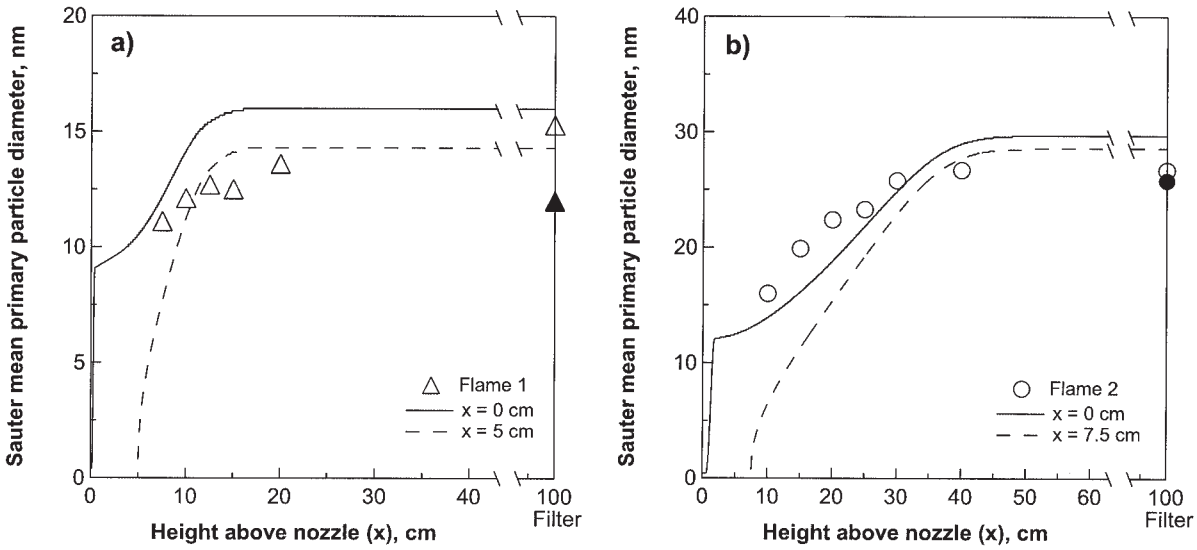

Figure 5. Calculated evolution of the primary particle Sauter mean diameter, d_{pS}, along the flame axis for (a) Flame 1 (triangles) and (b) Flame 2 (circles).

The open symbols are 500–3000 particle counts of TEM for each point, whereas filled symbols are nitrogen adsorption data at the filter. Additionally, the evolution of the d_{pS} by the proposed model is shown assuming instant droplet evaporation either at $x = 0$ (solid line) or at (a) $x = 5$ cm for Flame 1 and (b) $x = 7.5$ cm for Flame 2 (broken lines) corresponding to 2.5 cm below the lowest sampling points of Flames 1 and 2, respectively. The calculations predict well the evolution of the average primary particle diameter given the model assumptions (neglecting droplet evaporation and reaction, air entrainment, using integral line-of-sight temperature measurements and monodisperse primary and agglomerate particles).

slightly smaller (Flame 1) than the TEM-counted Sauter mean primary particle diameters. A similar particle diameter for BET and TEM as observed for Flame 2 (Figure 5b) indicates that the powders are nonagglomerated or only have a limited degree of agglomeration, in agreement with the TEM observations (Figure 3). Furthermore, the d_{pBET} is close to the tetragonal crystal size obtained from XRD (Mueller et al., 2004a), indicating that primary particles made from Flame 2 are only weakly (softly) agglomerated. Typically, in flame synthesis, where agglomerated product powders are formed, the average primary particle diameter obtained by TEM analysis is smaller than that obtained by BET N_2 adsorption because necking between the particles increases the corresponding BET particle diameter. For Flame 1 (Figure 5a), however, the d_{pBET} is slightly smaller than the Sauter mean primary particle diameter. This was also found in TiO_2 producing gas-fed premixed flames by Arabi-Katbi et al. (2001), who measured up to 20% lower SSAs for TiO_2 samples when using Ar as adsorption gas, consistent with Ross et al. (1988) for fumed silica powder. Another reason is that small highly agglomerated, sintered primary particles, which are observed at higher magnifications under TEM, are more difficult to count, which could thus lead to a larger TEM counted average primary particle compared to that obtained by BET.

The evolution of the primary particle geometric standard deviation σ_g as a function of x is shown in Figure 6. For Flame 2 (circles), the σ_g decreases steadily from 1.81 to 1.58 from $x =$ 10 to 40 cm, whereas for Flame 1 the σ_g decreases from 1.64 to 1.54 from $x = 7.5$ to 15 cm and then increases to 1.59 at $x =$ 20 cm. Decreasing the powder production rate from 300 to 100 g/h decreases the σ_g by about 10%, which is consistent with Kammler et al. (2003), who also observed that σ_g decreased when decreasing the TiO_2 powder production rate in gas-fed premixed flames. At the filter, the σ_g is 1.63 and 1.64 for Flames 2 and 1, respectively, in a similar range as found in gas-fed flame aerosol reactors (Arabi-Katbi et al., 2001; Kammler et al., 2003).

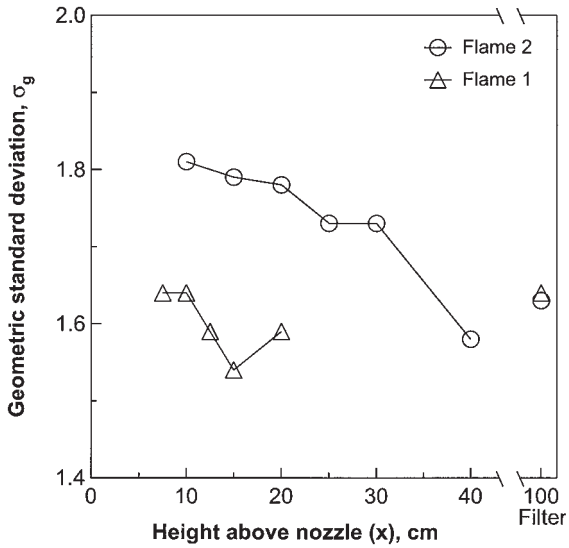

Figure 6. Evolution of the TS/TEM measured primary particle geometric standard deviation, σ_g, along the flame axis for ZrO_2 production rates of 100 (triangles, Flame 1) and 300 g/h (circles, Flame 2).

The σ_g of the PPSD at the end of the luminous part of the flame ($x = 12.5$ cm for Flame 1 and $x = 40$ cm for Flame 2) is not different from that collected on the filter. The σ_g decreases along the flame axis as coagulation–coalescence narrow early differences in particle size arising from differences from droplet evaporation times.

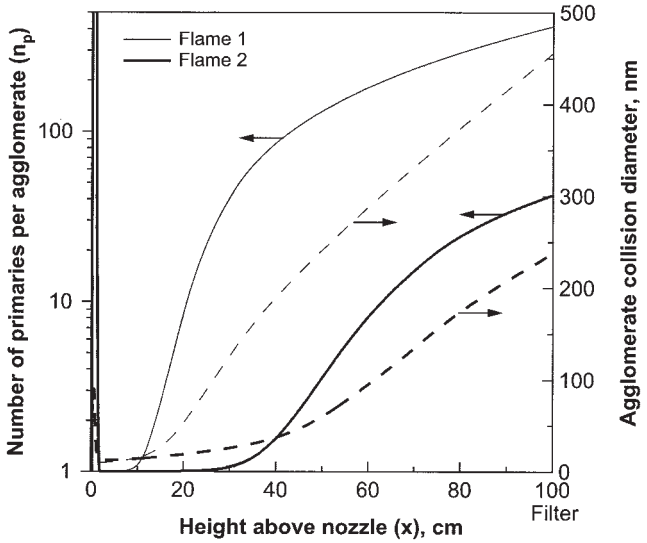

Figure 7. Number of ZrO_2 primary particles per agglomerate (solid lines) and agglomerate collision diameter (broken lines) along the centerline of the spray Flame 1 (thin lines) and 2 (thick lines) as predicted by the proposed model assuming instant droplet evaporation.

Agglomerates are formed after $x = 15$ and 40 cm, respectively, in Flames 1 and 2, consistent with TEM micrographs.

Particle dynamics and comparison with experimental data

Figure 5 shows also the evolution of the d_{pS} by the proposed model, assuming instant droplet evaporation either at $x = 0$ (solid lines) or at (a) $x = 5$ cm for Flame 1 and (b) $x = 7.5$ cm for Flame 2 (broken lines), corresponding to 2.5 cm below the lowest sampling point of each flame. The Sauter mean primary particle diameter made in Flames 1 and 2 are also shown in Figure 5. The choice of the location of the end of droplet evaporation affects the evolution of the Sauter mean primary particle diameter only at $x < 10$ and 20 cm for Flames 1 and 2, respectively. Later on in the spray flame, the primary particle diameter becomes quite similar (within 1 nm) regardless of the choice of that location.

For Flame 1 the two extreme evaporation conditions of the model bracket the measurements (Figure 5a), whereas for Flame 2 the model is closer to the data assuming instant ($x = 0$ cm) droplet evaporation. The model shows the d_{pS} growth in the region ($x < 30$ cm) of high temperatures (Figure 1), where sintering is enhanced and leads to an increase of the primary particle diameter until an asymptotic d_{pS} is attained above which primary particle growth stops (Figure 5). The TEM micrographs (Figures 2 and 3) imply that even further downstream agglomerates are formed, in accordance with the sharp increase of the average number of primary particles per agglomerate n_p, as well as the agglomerate collision diameter predicted from the model (Figure 7). The evolution of the primary particle diameter and that of the powder collected on the filter is predicted reasonably well by the proposed model (Figure 5), given its assumptions (neglecting droplet evaporation and reaction, air entrainment, using integral line-of-sight temperature measurements that may give lower than true temperature at the centerline, and monodisperse primary and agglomerate particles). For example, monodisperse coagulation-sintering models underpredict by about 10% accurate polydisperse ones in vapor-fed flame aerosol reactors (Tsantilis et al., 2002). Droplet evaporation seems to have little effect on ZrO_2 product particle characteristics at the present FSP conditions, as has also been observed for soot formation in liquid-fueled combustors (Fang et al., 1998). The agreement of model and data at the filter is surprisingly good for both production rates, given that particles of different growth history are collected there. Probably errors from the model assumptions compensate each other.

The degree of agglomeration reflected by the number of primary particles per agglomerate n_p is an important quality index in a number of applications. Figure 7 shows the evolution (along the centerline of the spray flame at starting condition $x = 0$ cm) of the number of ZrO_2 primary particles per agglomerate n_p (solid lines) and the ZrO_2 agglomerate collision diameter d_a (broken lines) for Flame 1 (thin lines) and Flame 2 (thick lines). For both production rates, agglomerates start to form very close ($x < 0.5$ cm) to the nozzle tip (Figure 7). Here, low to moderate temperatures (Figure 1) and high particle number concentrations prevail, promoting particle coagulation rather than rapid sintering. Compared to Flame 1, the temperature of Flame 2 is slightly lower close to the nozzle (Figure 1) and the particle number concentration is higher by a factor of 3, thus delaying precursor decomposition and the onset of agglomeration that increases the n_p (Figure 7).

Further downstream ($x \approx 2.5$ cm) as the spray flame temperature increases, agglomerates fully coalesce into spherical particles ($n_p = 1$) for both Flames 1 and 2, in agreement with TEM (Figures 2 and 3). Nevertheless, agglomeration takes over again ($n_p > 1$) following the steady decrease of temperature (Figure 1) and sintering rate ($x > 20$ cm for Flame 1 and $x > 40$ cm for Flame 2; Figure 7). The location in the spray flames where agglomeration takes over again (Figure 7) corresponds to spray flame temperatures of around 1000 K (Figure 1). The steep cooling of the spray flame with increasing x for Flame 1 (Figure 1) enhances agglomerate formation ($n_p \approx 400$), which is consistent with filter TEM (Figure 2f). For Flame 2, the present model predicts a lower n_p (around 40) than that of Flame 1 because the cooling rate of the spray is lower (Figure 1), leading to product powders with a lower degree of agglomeration.

At the same time as the n_p increases ($x = 20$–30 cm for Flame 1), the d_a increases as well (Figure 7). The n_p is much larger in Flame 1 than in Flame 2, leading to a larger d_a (Figure 7). This is consistent with TEM taken along the flame axis (such as Figure 2e vs. Figure 3c) but not with TEMs of the filter powders. The latter seem to have agglomerates of comparable size form both flames, regardless of production rate, although the model predicts that Flame 1 should give particles twice as large as those of Flame 2 at the filter. One possibility is that filter powders are a mixture of particles with different growth histories. Another possibility is that the model does not distinguish between hard and soft agglomerates (Tsantilis and Pratsinis, 2004). The latter can be broken during TEM sample preparation of the filter powders, thus obscuring the comparison of particle dynamics.

Of course, the evolution of the n_p is quite similar to calculations in gas-fed flame reactors (Tsantilis et al., 2002), given

that droplet evaporation and precursor release are neglected and may play an important role in particle growth during FSP, especially when hollow particles are produced. The degree of agglomeration along the flame axis, however, agrees well with TEM so the model can be used to guide reactor design and operation through the prediction of the degree of agglomeration and the agglomerate collision diameter. The model well describes the coagulation-controlled part of the spray flame and has to be extended to study the early formation and growth of the particles.

Conclusions

The growth of ZrO_2 particles in spray flames was investigated (1) experimentally by *in situ* thermophoretic sampling (TS) and counting 500–3000 particles by TEM image analysis at each sampling position in combination with Fourier transform infrared (FTIR) spectroscopy and (2) theoretically by a model accounting for aerosol coagulation and sintering, neglecting precursor evaporation, conversion, and particle polydispersity. Increasing the ZrO_2 powder production rate from 100 to 300 g/h increased the product primary particle diameter from 12 to 26 nm, in agreement with model predictions indicating that primary particle growth is dominated by coalescence. The geometric standard deviation of the primary particles, σ_g, decreased with increasing height above nozzle for both production rates, indicating that the difference in particle residence time histories from droplet evaporation and precursor release had resulted in broad particle size distributions early on in the flame. Further downstream, coagulation and sintering reduced the σ_g, whereas the size distribution of particles collected on the filter was broadened slightly again from the mixing between particles formed at different streamlines. The simple model predicted well the average primary particle diameter evolution, indicating that coagulation and sintering may determine solid particle formation in liquid-fed as well as in vapor-fed flame aerosol reactors, through the particle temperature history, residence time, and precursor concentration.

Acknowledgments

We acknowledge the financial support by the Swiss National Science Foundation (Grant 2100-063632.00/1) and partial support by the Swiss Commission for Technology and Innovation (KTI Project 5487.1). We thank Dr. M. Müller (ETH Zurich) for help with TEM.

Notation

A = total agglomerate area concentration, m^2/kg_{gas}
A_0 = initial area concentration of zirconia molecules, m^2/kg_{gas}
a = area of agglomerate particle, m^2
a_e = area of equivalent sphere to agglomerate of volume v, m^2
BET = Brunauer–Emmett–Teller
c = precursor concentration, M
D_b = grain boundary diffusion coefficient, m^2/s
D_f = mass fractal dimension
D_0 = grain boundary diffusion preexponential factor, m^2/s
d_a = agglomerate diameter, nm
d_n = average equivalent jet diameter, m
d_p = primary particle diameter, nm
d_{pBET} = BET-equivalent primary particle diameter, nm
d_{pS} = Sauter mean primary particle diameter, nm
$d_{50,3}$ = mass median diameter, μm
E = activation energy, J/mol
F = dispersion gas flow rate, L/min
FTIR = Fourier transform infrared
GLMR = gas-to-liquid mass ratio
IR = infrared
N = total zirconia number concentration, particles/kg_{gas}
N_A = Avogadro number, #/mol
N_0 = initial concentration of zirconia molecules, molecules/kg_{gas}
n_p = number of primary particles per agglomerate
PPSD = primary particle size distribution
R = universal gas constant, J mol^{-1} K^{-1}
r_p = sphere radius, m
S = liquid solution feed rate, mL/min
SSA = specific surface area, m^2/g
$T(0)$ = gas reference temperature, K
$T(x)$ = temperature, K
TEM = transmission electron microscopy
TS = thermophoretic sampling
t = time, s
u = axial average gas velocity, m/s
u_0 = exit gas velocity, m/s
V = total agglomerate volume concentration, m^3/kg_{gas}
V_0 = initial volume concentration of zirconia molecules, m^3/kg_{gas}
v = volume of agglomerate particle, m^3
w = grain boundary width, m
XRD = X-ray diffraction
x = axial distance from nozzle tip
x_n = neck length, m
Z = function

Greek letters

β = collision kernel between agglomerates, m^3/s
γ = surface tension, J/m^2
ρ_{gas} = gas density, kg/m^3
$\rho_{gas}(0)$ = gas density at T = 298 K, kg/m^3
ρ_p = particle density, kg/m^3
σ_g = geometric standard deviation of primary particles
τ_s = characteristic sintering time, s
Ω = molar volume, m^3/mol

Literature Cited

Akhtar, M. K., G. G. Lipscomb, and S. E. Pratsinis, "Monte Carlo Simulation of Particle Coagulation and Sintering," *Aerosol Sci. Technol.*, **21**, 83 (1994).

Arabi-Katbi, O. I., S. E. Pratsinis, P. W. Morrison, Jr., and C. M. Megaridis, "Monitoring the Flame Synthesis of TiO_2 Particles by In-Situ FTIR Spectroscopy and Thermophoretic Sampling," *Combust. Flame*, **124**, 560 (2001).

Bejan, A., *Convection Heat Transfer*, Wiley, New York (1984).

Best, P. E., R. M. Carangelo, J. R. Markham, and P. R. Solomon, "Extension of Emission-Transmission Technique to Particulate Samples Using FT-IR," *Combust. Flame*, **66**, 47 (1986).

Brossmann, U., R. Wurschum, U. Sodervall, and H. E. Schaefer, "Oxygen Diffusion in Ultrafine Grained Monoclinic ZrO_2," *J. Appl. Phys.*, **85**, 7646 (1999).

Byrne, G. D., "Pragmatic Experiments with Krylov Methods in the Stiff ODE Setting," *Computational Ordinary Differential Equations*, J. Cash and I. Gladwell, eds., Oxford University Press, Oxford, UK, pp. 323–356 (1992).

Chraska, T. A., H. King, and C. C. Berndt, "On the Size-Dependent Phase Transformation in Nanoparticulate Zirconia," *Mater. Sci. Eng. A Struct. Mater. Properties Microstruct. Process.*, **286**, 169 (2000).

Coblenz, W. S., J. M. Dynys, R. M. Cannon, and R. L. Coble, "Initial Stage Solid State Sintering Models. A Critical Analysis and Assessment," *Sintering Processes: Material Science Research*, G. C. Kuczynski, ed., Plenum, New York, pp. 141–157 (1980).

Dobbins, R. A., and C. M. Megaridis, "Morphology of Flame-Generated Soot as Determined by Thermophoretic Sampling," *Langmuir*, **3**, 254 (1987).

Fang, T. C., C. M. Megaridis, W. A. Sowa, and G. S. Samuelsen, "Soot Morphology in a Liquid-Fueled, Swirl-Stabilized Combustor," *Combust. Flame*, **112**, 312 (1998).

Gell, M., "Application Opportunities for Nanostructured Materials and Coatings," *Mater. Sci. Eng. A Struct. Mater. Properties Microstruct. Process.*, **204**, 246 (1995).

Gleiter, H., "Materials with Ultrafine Microstructures: Retrospectives and Perspectives," *Nanostruct. Mater.*, **1**, 1 (1992).
Hinds, W. C., *Aerosol Technology*, Wiley, New York (1999).
Johannessen, T., S. E. Pratsinis, and H. Livbjerg, "Computational Fluid-Particle Dynamics for the Flame Synthesis of Alumina Particles," *Chem. Eng. Sci.*, **55**, 177 (2000).
Kammler, H. K., "Synthesis of Oxide Nanoparticles with Closely Controlled Characteristics," PhD Thesis, Eidgenössiche Technische Hochschule (ETH, Swiss Federal Institute of Technology), Zurich, Switzerland (2002).
Kammler, H. K., R. Jossen, P. W. Morrison, Jr., S. E. Pratsinis, and G. Beaucage, "The Effect of External Electric Fields during Flame Synthesis of Titania," *Powder Technol.*, **135**, 310 (2003).
Kammler, H. K., R. Mueller, O. Senn, and S. E. Pratsinis, "Synthesis of Silica–Carbon Particles in a Turbulent H_2–Air Flame Aerosol Reactor," *AIChE J.*, **47**, 1533 (2001).
Kammler, H. K., S. E. Pratsinis, P. W. Morrison, Jr., and B. Hemmerling, "Flame Temperature Measurements during Electrically Assisted Aerosol Synthesis of Nanoparticles," *Combust. Flame*, **128**, 369 (2002).
Karthikeyan, J., C. C. Berndt, J. Tikkanen, J. Y. Wang, A. H. King, and H. Herman, "Nanomaterial Powders and Deposits Prepared by Flame Spray Processing of Liquid Precursors," *Nanostruct. Mater.*, **8**, 61 (1997).
Kilian, A., and T. F. Morse, "A Novel Aerosol Combustion Process for the High Rate Formation of Nanoscale Oxide Particles," *Aerosol Sci. Technol.*, **34**, 227 (2001).
Kobata, A., K. Kusakabe, and S. Morooka, "Growth and Transformation of TiO_2 Crystallites in Aerosol Reactor," *AIChE J.*, **37**, 347 (1991).
Koch, W., and S. K. Friedlander, "Particle Growth by Coalescence and Agglomeration," *Particle & Particle Syst. Charact.*, **8**, 86 (1991).
Kodas, T. T., and M. J. Hampden-Smith, *Aerosol Processing of Materials*, Wiley–VCH, New York (1999).
Kruis, F. E., K. A. Kusters, S. E. Pratsinis, and B. Scarlett, "A Simple Model for the Evolution of the Characteristics of Aggregate Particles Undergoing Coagulation and Sintering," *Aerosol Sci. Technol.*, **19**, 514 (1993).
Laine, R. M., R. Baranwal, T. Hinklin, D. Treadwell, A. Sutorik, C. Bickmore, K. Waldner, and S. S. Neo, "Making Nanosized Oxide Powders from Precursors by Flame Spray Pyrolysis," *Key Eng. Mater.*, **159–160**, 17 (1999)
Laine, R. M., T. Hinklin, G. Williams, and S. C. Rand, "Low-Cost Nanopowders for Phosphor and Laser Applications by Flame Spray Pyrolysis," *J. Metastable Nanocryst. Mater.*, **8**, 500 (2000).
Limaye, A. U., and J. J. Helble, "Morphological Control of Zirconia Nanoparticles through Combustion Aerosol Synthesis," *J. Am. Ceram. Soc.*, **85**, 1127 (2002).
Limaye, A. U., and J. J. Helble, "Effect of Precursor and Solvent on Morphology of Zirconia Nanoparticles Produced by Combustion Aerosol Synthesis," *J. Am. Ceram. Soc.*, **86**, 273 (2003).
Madeyski A., and W. W. Smeltzer, "Oxygen Diffusion in Monoclinic Zirconia," *Mater. Res. Bull.*, **3**, 369 (1968)
Mädler, L., H. K. Kammler, R. Mueller, and S. E. Pratsinis, "Controlled Synthesis of Nanostructured Particles by Flame Spray Pyrolysis," *J. Aerosol Sci.*, **33**, 369 (2002).
Mädler, L., and S. E. Pratsinis, "Bismuth Oxide Nanoparticles by Flame Spray Pyrolysis," *J. Am. Ceram. Soc.*, **85**, 1713 (2002).
Marshall, B. S., I. Telford, and R. Wood, "A Field Method for the Determination of Zinc Oxide Fume in Air," *Analyst*, **96**, 569 (1971).
Mayo, M. J., J. R. Seidensticker, D. C. Hague, and A. H. Carim, "Surface Chemistry Effects on the Processing and Superplastic Properties of Nanocrystalline Oxide Ceramics," *Nanostruct. Mater.*, **11**, 271 (1999).
Mueller, R., "Characterization and Synthesis of Nanoparticles Made in Vapor and Spray Flames," PhD Thesis, Eidgenössiche Technische Hochschule (ETH, Swiss Federal Institute of Technology), Zurich, Switzerland (2003).
Mueller, R., R. Jossen, S. E. Pratsinis, M. Watson, and M. K. Akhtar, "Zirconia Nanoparticles Made in Spray Flames at High Production Rates," *J. Am. Ceram. Soc.*, **87**, 197 (2004a).
Mueller, R., H. K. Kammler, S. E. Pratsinis, A. Vital, G. Beaucage, and P. Burtscher, "Non-Agglomerated Dry Silica Particles," *Powder Technol.*, **140**, 40 (2004b).
Mueller, R., L. Mädler, and S. E. Pratsinis, "Nanoparticle Synthesis at High Production Rates by Flame Spray Pyrolysis," *Chem. Eng. Sci.*, **58**, 1969 (2003).
Nakaso, K. K., K. Okuyama, M. Shimada, and S. E. Pratsinis, "Effect of Reaction Temperature on CVD-Made TiO_2 Primary Particle Diameter," *Chem. Eng. Sci.*, **58**, 3327 (2003).
Pratsinis, S. E., "Flame Aerosol Synthesis of Ceramic Powders," *Prog. Energy Combust. Sci.*, **24**, 197 (1998).
Pratsinis, S. E., O. Arabi-Katbi, C. M. Megaridis, P. W. Morrison, Jr., S. Tsantilis, and H. K. Kammler, "Flame Synthesis of Spherical Nanoparticles," *J. Metastable Nanocryst. Mater.*, **8**, 511 (2000).
Rösner-Kuhn, M., W. H. Hofmeister, G. Kuppermann, R. J. Bayuzick, and M. G. Frohberg, "Investigations of the Influence of Oxygen on the Surface Tension of Zirconium by the Oscillating Drop Technique," *Surf. Sci.*, **443**, 159 (1999).
Ross, S. B., D. M. Smith, A. J. Hurd, and D. W. Schaefer, "Surface Roughness in Vapor-Phase Aggregates via Adsorption and Scattering Techniques," *Langmuir*, **4**, 977 (1998).
Schaefer, D. W., and A. J. Hurd, "Growth and Structure of Combustion Aerosols—Fumed Silica," *Aerosol Sci. Technol.*, **12**, 876 (1990).
Seinfeld, J. H., *Atmospheric Chemistry and Physics of Air Pollution*, Wiley, New York (1986).
Sokolowski, M., A. Sokolowska, A. Michalski, and B. Gokieli, "The 'In-Flame-Reaction' Method for Al_2O_3 Aerosol Formation," *J. Aerosol Sci.*, **8**, 219 (1977).
Spicer, P. T., O. Chaoul, S. Tsantilis, and S. E. Pratsinis, "Titania Formation by $TiCl_4$ Gas Phase Oxidation, Surface Growth and Coagulation," *J. Aerosol Sci.*, **33**, 17 (2002).
Strobel, R., W. J. Stark, L. Mädler, S. E. Pratsinis, and A. Baiker, "Flame-Made Platinum/Alumina: Structural Properties and Catalytic Behaviour in Enantioselective Hydrogenation," *J. Catal.*, **213**, 296 (2003).
Tani, T., K. Takatori, N. Watanabe, and N. Kamiya, "Metal Oxide Powder Synthesis by the Emulsion Combustion Method," *J. Mater. Res.*, **13**, 1099 (1998).
Tani, T., N. Watanabe, K. Takatori, and S. E. Pratsinis, "Morphology of Oxide Particles Made by the Emulsion Combustion Method," *J. Am. Ceram. Soc.*, **86**, 898 (2003).
Tsantilis, S., H. K. Kammler, and S. E. Pratsinis, "Population Balance Modeling of Flame Synthesis of Titania Nanoparticles," *Chem. Eng. Sci.*, **57**, 2139 (2002).
Tsantilis, S., and S. E. Pratsinis, "Soft-, Hard-, and Non-Agglomerated Aerosols Made at High Temperatures," *Langmuir*, **20**, 5933 (2004).

Manuscript received Oct. 3, 2003, and revision received Apr. 6, 2004.